Astronomy & Astrophysics manuscript no. output
July 17, 2023

Wavelet determination of magnetohydrodynamic range power spectral exponents in solar wind turbulence seen by Parker Solar Probe

X. Wang[1], S. C. Chapman[1 2 3], R. O. Dendy[1], and B. Hnat[1]

[1] Centre for Fusion, Space and Astrophysics, Physics Department, University of Warwick, Coventry CV4 7AL, UK
[2] Department of Mathematics and Statistics, University of Tromsø, Norway
[3] International Space Science Institute, Bern, Switzerland

July 17, 2023

ABSTRACT

Context. The high Reynolds number solar wind flow provides a natural laboratory for the study of turbulence in-situ. Parker Solar Probe samples the solar wind between 0.17 AU to 1 AU, providing an opportunity to study how turbulence evolves in the expanding solar wind.
Aims. To obtain estimates of the scaling exponents and scale breaks of the power spectra of magnetohydrodynamic (MHD) turbulence at sufficient precision to discriminate Kolmogorov from Iroshnikov-Kraichnan (IK) turbulence, both within each spectrum and across multiple samples at different distances from the Sun and at different plasma β.
Methods. We identified multiple, long-duration intervals of uniform solar wind turbulence, sampled by PSP/FIELDS, selected to exclude coherent structures such as pressure pulses and current sheets, and in which the primary proton population velocity varies by less than 20% of its mean value. The local value of plasma β for these datasets spans the range $0.14 < \beta < 4$. All selected events span the spectral scales from the approximately '$1/f$' range at low frequencies, through the MHD inertial range (IR) of turbulence and into the kinetic range, below the ion gyrofrequency. We estimate the power spectral density (PSD) using a discrete Haar wavelet decomposition which provides accurate estimates of the IR exponents.
Results. Within 0.3 AU from the sun, the IR exhibits two distinct ranges of scaling. The inner, high frequency range has an exponent consistent with IK within uncertainties. The outer, low frequency range is shallower, with exponents in the range between -1.37 and -1.23. Between 0.3 and 0.5 AU, the IR exponents are closer to, but steeper than, IK and do not coincide with the value -3/2 within uncertainties. At distances beyond 0.5 AU from the Sun, the exponents are close to, but mostly steeper than, Kolmogorov -5/3: uncertainties inherent in the observed exponents exclude the value -5/3. Between these groups of spectra we find examples, 0.26 AU and at 0.61 AU, two distinct IR ranges of scaling. The inner, high frequency range has an exponent ~ -1.4 and the low frequency range has an exponent close to Kolmogorov -5/3.
Conclusions. Since the PSD estimated scaling exponents are a central prediction of turbulence theories, these results provide new insights into our understanding of the evolution of turbulence in the solar wind.

Key words. Solar wind, turbulence, Parker Solar Probe

1. Introduction

The high Reynolds number solar wind flow provides a natural laboratory for the study of turbulence in situ. A wealth of observations at 1 AU has established that there is a well-defined magnetohydrodynamic (MHD) inertial range (IR) of turbulence that can be seen in the power spectral density of the magnetic field (Verscharen et al. 2019; Tu & Marsch 1995; Kiyani et al. 2015), in the non-Gaussian probability density of fluctuations (Bruno et al. 2004; Sorriso-Valvo et al. 2015; Chen 2016) and in the scaling properties of higher order statistics, such as kurtosis (Feynman & Ruzmaikin 1994; Hnat et al. 2011) and structure functions (Horbury & Balogh 1997; Chapman et al. 2005; Chapman & Hnat 2007). This MHD IR terminates at approximately the ion gyro-period on short timescales (Kiyani et al. 2013; Chen 2014) and on long timescales is bracketed by an approximately '$1/f$' region, presumably of solar origin (Matthaeus et al. 2007; Nicol et al. 2009; Gogoberidze & Voitenko 2016).

Hydrodynamic turbulence, under idealized conditions of isotropy, homogeneity, and incompressibility, is universal in that the IR power law power spectral exponent of $-5/3$ (Kolmogorov 1941) is constrained by dimensional analysis, see e.g. (Buckingham 1914; Longair 2003; Barenblatt 1996; Chapman & Hnat 2007). MHD turbulence on the other hand has anomalous scaling (Politano & Pouquet 1995; Salem et al. 2009); the number of relevant parameters is such that, unlike ideal hydrodynamic turbulence, the spectral exponent is not constrained by dimensional analysis and may vary with plasma conditions and the underlying phenomenology. There has thus been longstanding interest in determination of the power spectral exponent of the IR turbulence. Theoretical predictions for MHD IR turbulence give exponents ranging from $-5/3$ to $-3/2$ (Kraichnan 1965; Iroshnikov 1964; Goldreich & Sridhar 1995; Verma 1999; Zhou et al. 2004), highlighting the importance of data analysis methodology that can discriminate between values within this range.

The IR of solar wind turbulence is known to evolve with the distance from the Sun. Early measurements by Helios established that the low frequency transition from the '$1/f$' to the IR increases with heliospheric distance (Bruno & Carbone 2013; Tu & Marsch 1995). Scaling and anisotropy have been examined us-

ing planetary probes (Wicks et al. 2010). The Parker Solar Probe (PSP) (Fox et al. 2016) samples the solar wind between 0.16 AU to 1 AU, providing an unprecedented opportunity to study the evolution of turbulence in the expanding solar wind. Surveys of power spectra of multiple PSP observations confirm an evolution in the extent of the IR and suggest a drift in the exponent of the power spectrum (Chen et al. 2020; Alberti et al. 2020) from $-5/3$ at 1 AU to $-3/2$ closer to the Sun. These surveys have mostly relied on discrete Fourier transform (DFT) estimates of the power spectral density, however see also Alberti et al. (2020), Sioulas et al. (2023) and Davis et al. (2023) for other methods. In this paper we use a discrete wavelet transform (DWT) to estimate the power law exponents of the power spectral density (PSD) of the magnetic field in the IR of solar wind turbulence. Whilst any decomposition can in principle be used to estimate the PSD, we consider that wavelets are optimal here because they partition the frequency domain into intervals whose spacing is intrinsically power law, as distinct from the linearly spaced intervals of the DFT. Whereas DWT based estimates of the power spectrum usually involve averaging over the PSDs obtained from multiple sub-intervals of data, as in Welch's method (Welch 1967) the wavelet based PSD estimates here require no such averaging.

Once an estimate of the PSD has been obtained, a power law model is fitted over a finite range of frequencies within the observed PSD. Central to accurate fitting of power laws is to determine the appropriate range of frequencies over which to perform the fitting procedure, that is, to identify the location of the scale breaks. Here, we develop a non-parametric procedure for identifying the scale breaks, and then obtain estimates, with uncertainties, of the power law exponents for the distinct ranges in the PSD that these scale breaks discriminate.

The paper is organized as follows. In Section 2 we present the datasets and describe how the wavelet PSDs are first obtained, the procedure by which we identify power law PSD breakpoints, and then how the power law exponents are obtained by finite range power law fits to the PSD. In Section 3, we present detailed examples of the application of these techniques to four selected PSP datasets taken between 0.17 AU and 0.70 AU, together with a Table of results for further 17 PSP datasets. Taken together, this portfolio of results enables us to determine the dependence of the spectral exponents and of spectral breakpoint locations on the value of local plasma β and on the distance from the Sun. Our conclusions are summarised in Section 4.

2. Methods

2.1. Data Selection

We identify multiple, long-duration intervals of uniform solar wind turbulence observed by PSP/FIELDS, selected to exclude coherent structures such as current sheets and pressure pulses. All selected events span the spectral scales from the approximately '$1/f$' range at low frequencies, through the MHD IR of turbulence and into the kinetic range, below the ion gyrofrequency. We will only include in our study, events which have a clear '$1/f$' range of scaling in addition to an IR and a kinetic range.

Our analysis focuses on magnetic field measurements from the fluxgate magnetometer (MAG), which is a part of the FIELDS suite (Bale et al. 2016). The cadence of MAG measurements is 0.437 second. All vectors quantities are in the RTN coordinates (where R is in the ecliptic plane and points from the Sun to the spacecraft, T is the vector cross product of the rotation vector of the Sun with R, and N which is the vector cross product of R with T completes the right-handed orthonormal triad). Seventeen quiet periods are analysed, in which large-scale coherent structures are absent and the proton population velocity varies by less than 20% of its mean value. We use Level 3 data from the PSP solar-facing Faraday cup on board of SWEAP (Kasper et al. 2016) instrument suite to infer plasma moments. We obtain estimates of the scaling exponents of the trace of the power spectral tensor (Wicks et al. 2012) of these selected intervals. Estimates of the power law spectral exponents have previously been obtained using Fourier estimates of the spectra (Sioulas et al. 2023). These require averaging over multiple spectra to reduce scatter, and to obtain an uncertainty estimate (Welch 1967). Here, we will use wavelets to estimate the power law spectral exponents of individual intervals of data, together with their uncertainty, without recourse to averaging.

2.2. Spectral Estimation Using Wavelets

We estimate the power spectral density (PSD) using a Haar undecimated discrete wavelet transform (UDWT, see e.g. (Kiyani et al. 2013). This has the following desirable properties. First, the width of the j^{th} frequency interval over which the spectrum is estimated is 2^j times the smallest frequency interval, which in turn is set by the time resolution of the observations. The central frequencies of estimates of the PSD are thus linearly spaced on a logarithmic scale, hence they uniformly populate a finite range of a power law PSD wavelets over which we then fit a power law function. Second, the set of Haar wavelets is complete and orthonormal. As a consequence, a power law PSD can be resolved to good fidelity by a single Haar DWT across a given time interval. To achieve the same precision with the DFT would require averaging over multiple spectra obtained from sub-samples in time over the interval, with corresponding loss of frequency range, as in Welch's method (Welch 1967). With the DWT it is thus easier to obtain PSD estimates that span the '$1/f$' range, IR and DR as here. We have previously demonstrated this with simple modelling (Wang et al. 2022), which shows in particular that for realistic data samples, the Haar wavelet spectra can discriminate between $-5/3$ and $-3/2$ scaling exponents within uncertainties.

The power spectral exponents are obtained by linear least-squares regression of the power law ranges of the PSD when plotted on a log-log scale. Accurate determination of the endpoints of the power law ranges in the spectra is central to obtaining accurate estimates of the exponents. This is achieved by an iterative procedure based on evaluation of the error on the least-squares linear fit to the gradient of a succession of series of neighbouring points on the DWT-estimated spectrum. Our approach is simple: if the error significantly worsens on adding the $(n+1)$th point to a sequence previously extending only to the nth point, this suggests the existence of a breakpoint located between the nth and $(n+1)$th points. One can then continue, fitting a different gradient to a new set of sequences beginning at the $(n+1)$th point, and perhaps finding a further breakpoint if the error suddenly increases when the $(n+m)$th point, say, is included. It is important, for consistency, to perform this series of operations in both directions. That is, sequentially adding points in the direction from higher to lower frequency, and having completed this, back again from lower to higher. This approach is embodied in the algorithm described below, steps 1 to 8, and examples are shown in Figs. 1 and 2.

We consider a finite range power law region of the PSD, $U_{k,m}$ comprised of wavelet power estimates $W_k, W_{k+1}, ..., W_m$ estimated at each wavelet scale $j = k, k+1, ..., m$, at central fre-

quencies f_j. Higher values of j correspond to lower frequencies. Each estimate of the power spectral exponent based on $U_{k,m}$ will have uncertainty $\epsilon_{k,m}$. We obtain both the value of the power spectral exponent and its uncertainty from a linear least squares fit to the sequence of W_j, f_j in the $U_{k,m}$ region.

The following procedure is used to estimate the frequencies of the upper and lower bounds of the power law range of scaling, at breakpoint frequencies f_P and f_Q.

1. Estimate the power spectral exponent from $U_{k,k+l}$ where wavelet temporal scale k lies within the power law region of the PSD at central frequency f_k.
2. Successively increase the frequency range, in the direction of decreasing frequency, by considering $l = 1, 2, 3, ...$ and at each value of l estimate the power spectral exponent.
3. Test if $\epsilon_{k,k+l} > \epsilon_{k,k+l+1}$, if true, increment l.
4. If $\epsilon_{k,k+l} < \epsilon_{k,k+l+1}$ then the low frequency breakpoint $Q = k+l$ has been reached.
5. Now estimate the power spectral exponent from $U_{Q-l,Q}$.
6. Successively increase the frequency range, in the direction of increasing frequency, by considering $l = 1, 2, 3, ...$ and at each value of l estimate the power spectral exponent.
7. Test if $\epsilon_{Q-l,Q} > \epsilon_{Q-l-1,Q}$, if true, increment l.
8. If $\epsilon_{Q-l,Q} < \epsilon_{Q-l-1,Q}$ then the high frequency breakpoint $k = Q - l = P$ has been reached.

In this paper, we have only considered intervals of PSP data where there is a clearly identifiable transition between the IR and the '$1/f$' range. However, we find that these do not all correspond to the simple case outlined in the preceding paragraph. In particular, our procedure has identified cases where the low frequency breakpoint Q is clearly at a higher frequency than the transition between the IR and '$1/f$' range. Examples are shown in Figs. 3 and 4. In these cases we have applied the above procedure to search for the IR-'$1/f$' transition as follows:

1. Estimate the power spectral exponent from $U_{Q,Q+l}$ where wavelet temporal scale $k = Q$ has been determined as above.
2. Successively increase the frequency range by considering $l = 1, 2, 3, ...$ and at each value of l estimate the power spectral exponent.
3. Test if $\epsilon_{Q,Q+l} > \epsilon_{Q,Q+l+1}$, if true, increment l.
4. If $\epsilon_{Q,Q+l} < \epsilon_{Q,Q+l+1}$ then the low frequency breakpoint $m = Q + l = R$ has been reached.

This determines wavelet scale R and frequency f_R as an upper limit on the transition between the IR and the '$1/f$' range.

Once a power law range is identified in the PSD, a linear least squares fit is performed in log-log space to obtain the spectral exponent and the fit uncertainty, here we quote 95 percent confidence bounds on the fitted power spectral exponent throughout.

3. Results

3.1. Example spectra

We have applied the above procedure to PSP intervals, selected across a wide range of radial distances from the Sun, hence across a correspondingly wide range of values of the local plasma β. We have found that the spectra can be classified into four types which order their overall morphology. These are: Type I which can be fitted by two ranges of scaling within the inertial range, the inner, high frequency range has exponent close to IK, whereas the low frequency range is shallower. Type II can be fitted by a single inertial range of scaling with exponents between the IK and Kolmogorov values, Type III which can be fitted by two ranges of scaling within the inertial range, the inner, high frequency range has exponent close to Kolmgorov, whereas the low frequency range is shallower. Finally Type IV which can be fitted by a single inertial range of scaling with exponents close to Kolmogorov. We will see that this classification is ordered with distance from the sun. In all cases, a clear transition to the '1/f' range of scaling is identified in the spectra.

We will first plot the PSD for four intervals representing each of these types, at different heliospheric distances, to illustrate the procedure for identifying ranges of power law variation in the PSD, and estimation of the power spectral exponents.

The top panels of Figs. 1 to 4 plot the DWT estimates of the PSD for the trace of the power spectral tensor. Different colours and symbols are used to indicate the distinct power law ranges where they can be identified using the method described above. Where a clear '$1/f$' (that is, f^α, where the index α is some negative number) range can be identified, it is indicated by black triangles. The IR is indicated by diamonds where pink indicates a scaling exponent close to Kolmogorov $\alpha = -5/3$, and blue, a scaling exponent close to IK $\alpha = -3/2$.

The dissipation range, and in many cases the '$1/f$' range, are not fully resolved as distinct power law ranges in these observations; nevertheless, they are clearly identified as being outside of the IR by the breakpoint finding procedure. These points are indicated by grey asterisks on the plots.

The DWT temporal scales j converted to frequencies $f = f_0 2^{-j}$ Hz where $f_0 = 1/(2dt)$ Hz, (dt is the cadence of the observations), are numbered at the top of these panels. The wavelet temporal scales at which breakpoints are identified by the above iterative procedures are indicated on the spectra. The iterative procedure is summarized for each of these spectra in the schematic (centre panel). Fig. 1 obtains the IR power law spectral exponent for an interval of turbulent solar wind of 12-hour duration at heliospheric distance 0.5 AU and for $\beta = 0.53$.

In Fig. 1, the procedure begins at the wavelet temporal scale labelled "Start", and is first applied along the path labelled (i) from higher to lower frequencies to determine the low-frequency end of the IR (Q) which is a transition to the '$1/f$' range. It is then applied along the path labelled (ii) from lower frequencies to higher, to determine the high-frequency end of the IR (P) which is a transition to the kinetic range. The fitted power law exponent and its uncertainty for each iteration are plotted in the last two panels, for each sequence of iterations (i) and (ii). As more wavelet scales are successively included in the fitting range, the uncertainty decreases. The uncertainty remains small, and the value of the fitted exponent remains constant until the fitting range extends beyond the power-law range of the spectrum. For comparison, horizontal dashed lines indicate power-law scaling exponents of $\alpha = -3/2$ and $\alpha = -5/3$ and we can see that for this interval of turbulent solar wind, the scaling is clearly identified as between IK $\alpha = -3/2$ and Kolmogorov $\alpha = -5/3$. In this case, the '$1/f$' range is discerned at lower frequencies and is clearly distinct from the IR.

Fig. 2 shows the spectrum obtained for an interval of the turbulent solar wind of 3-hour duration at heliospheric distance 0.7 AU and for $\beta = 3.71$. In this case, our procedure identifies a single scaling region, but the scaling exponent now approximates Kolmogorov $\alpha = -5/3$ scaling. In this case, the interval is not long enough to fully resolve a clear power law '$1/f$' range. Our method identifies all breakpoints in the wavelet spectra, without assuming the existence of specific power law ranges. We have found cases where the spectra are well described by an IR composed of two power-law regions with distinct scaling exponents. Two examples are presented in Figs. 3 and 4, which correspond

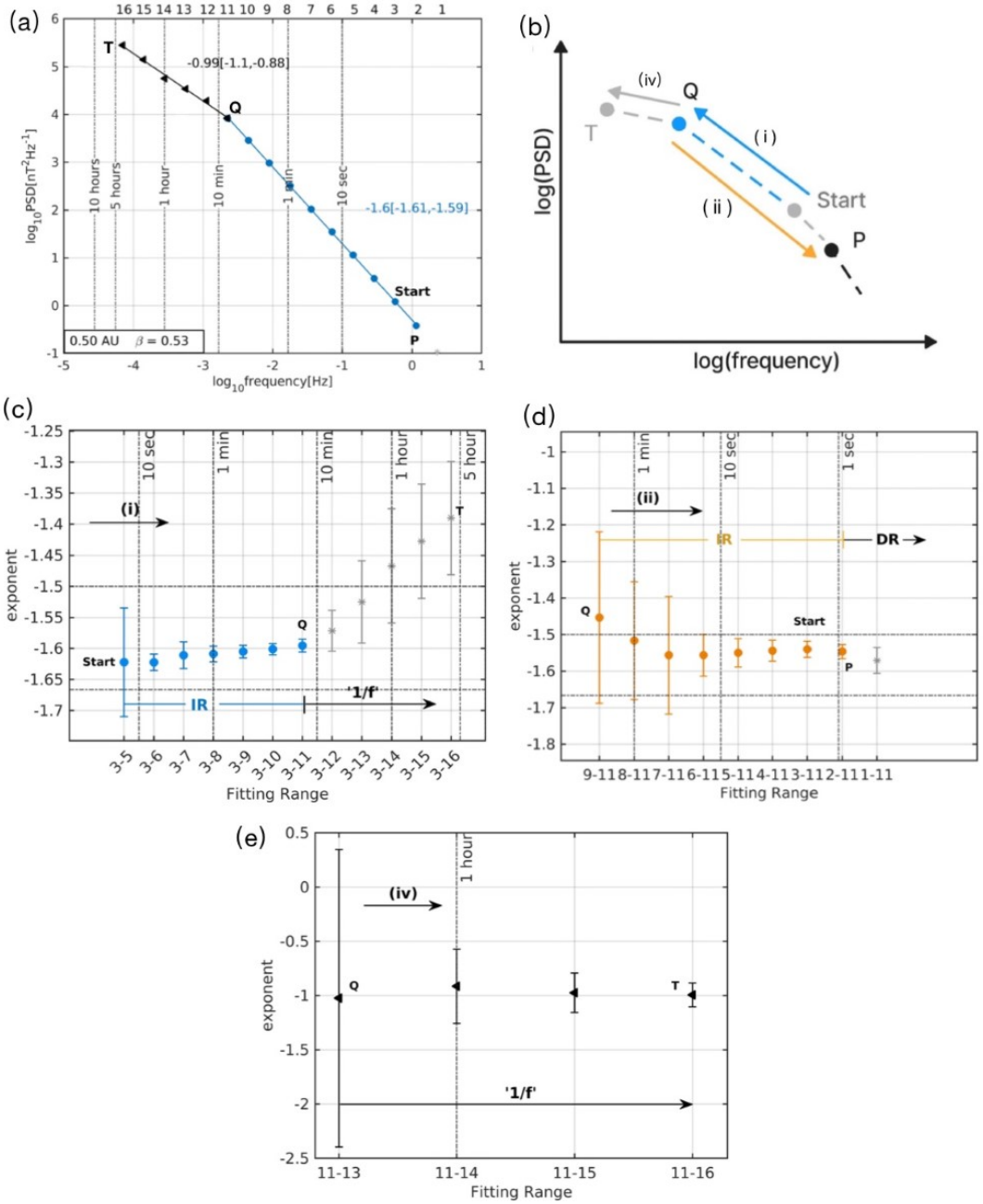

Fig. 1: Example of a type II spectrum which shows a single range of close to IK scaling across the full IR for PSP/FIELDS measurements of the full trace of power spectral tensor, taken over a 12-hour interval at 0.5 AU with local plasma $\beta = 0.53$. (**a**): Log-log plot of power spectral density versus frequency: plotted points result from Haar wavelet analysis of the dataset, these are marked as blue circles in the IR identified here, grey asterisks outside it. (**b**): Procedural diagram for the two adjacent scatter plots, used to identify the IR and its single best-fit gradient. The first (counting from the right) blue circle is labelled P; the second, "Start"; the eleventh, Q; there follow six black triangles, and the last one is labelled T. Breakpoints at the upper and lower end of the IR are identified by locating sudden increases in the 95% confidence interval (CI) of the exponent using the method of Sec.2.2, as shown in the two lowest panels, as follows. (**c**): Spectral exponent and its CI, on the blue pathway labelled (i) beginning at "Start" and ending at Q in the procedural diagram above. (**d**): The same, but for the yellow pathway labelled (ii) beginning at Q and descending to the first blue circle P. (**e**): CI for pathway (iv) shows that the '$1/f$' range continues to the sixteenth point, labelled T.

to an interval of 5-hour duration with local plasma $\beta = 1.02$ at 0.61 AU and a 48-hour interval with local plasma $\beta = 0.34$ at 0.17 AU, respectively.

In Fig. 3 the IR is best fitted by a power law range from wavelet scale 2 to scale 7 (temporal scales from 0.9 sec to 28.0 sec, with corresponding frequencies spanning from 0.04 Hz to 1.11 Hz) where the scaling is close to Kolmogorov, the fitted line is of exponent -1.73 [-1.75, -1.71], and a second power law from wavelet scale 7 to scale 13 (temporal scales from 28.0 sec to 30.0 min, with corresponding frequencies spanning from 5.56×10^{-4} Hz to 0.04 Hz) with exponent -1.39 [-1.47, -1.31]. This identifies a break in scaling at about 30 seconds within the IR, with the full

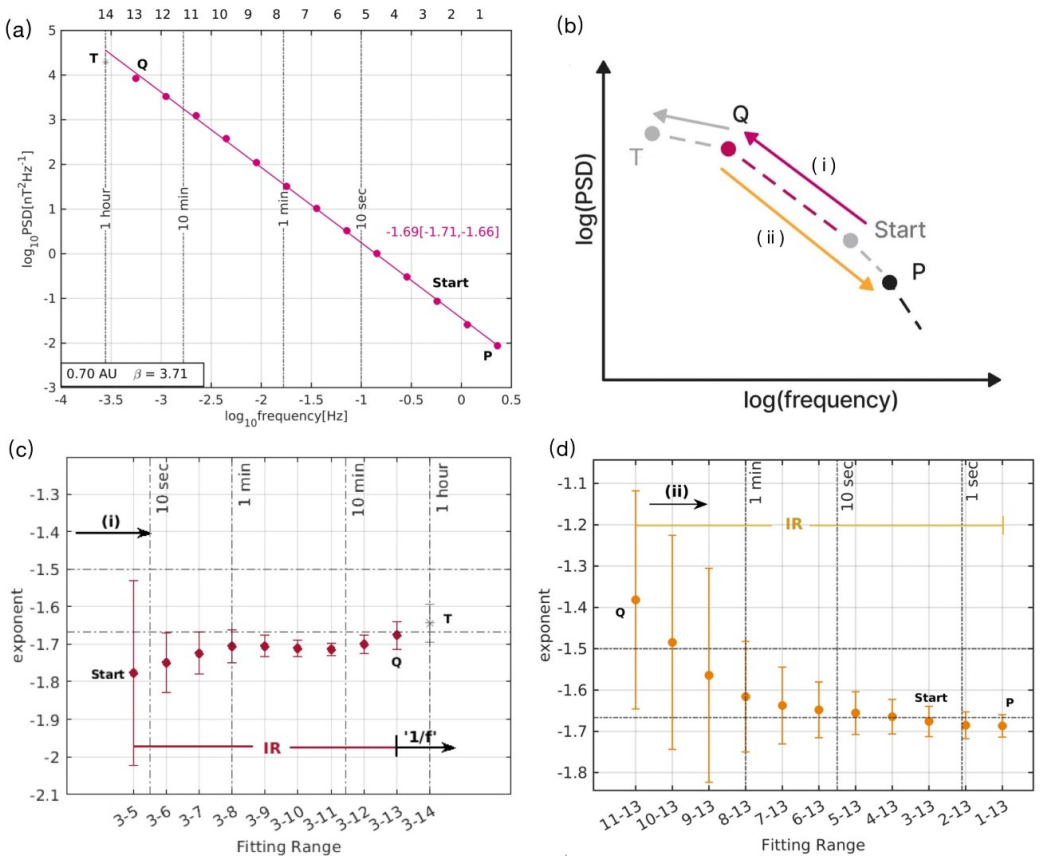

Fig. 2: Example of a type IV spectrum which shows a single range of scaling close to Kolmogorov across the full IR for PSP/FIELDS measurements of the full trace of power spectral tensor, taken over a 3-hour interval at 0.70 AU with local plasma $\beta = 3.71$. (**a**): Log-log plot of power spectral density versus frequency: plotted points result from Haar wavelet analysis of the dataset, these are marked as red circles in the IR identified here, a grey asterisk outside it. (**b**): Procedural diagram for the two adjacent scatter plots, used to identify the IR and its single best-fit gradient. The first (counting from the right) red circle is labelled P; the first, "Start"; the thirteenth, Q; there follows a grey asterisk, labelled T. Breakpoints at the upper and lower end of the IR, are identified by locating sudden increases in the CI of the exponent using the method of Sec.2.2, as shown in the two lowest panels, as follows. (**c**): Spectral exponent and its CI, on the red pathway labelled (i) beginning at "Start" and ending at Q in the procedural diagram above. (**d**): The same, but for the yellow pathway labelled (ii) beginning at Q and descending to the first red circle P.

IR occupying the range from wavelet scale 2 to scale 13, that is, from approximately 0.9 sec to about 30.0 min, with corresponding frequencies spanning from 5.56×10^{-4} Hz to 1.11 Hz. To illustrate this, we have extended the fitted line from wavelet scales from scale 7 to scale 13, (temporal scales from 28.0 sec to 30.0 min, with corresponding frequencies spanning from 5.56×10^{-4} Hz to 0.04 Hz). It is clear that for timescales longer than scale 8, or about 1 minute, the observed spectrum progressively deviates from the fitted line. A second example is provided in Fig. 4 where wavelet scale 3 to scale 8 (temporal scales from 1.8 sec to 1 min, with corresponding frequencies spanning from 1.67×10^{-2} Hz to 0.56 Hz) follow IK scaling within narrow error bars (gradient = -1.52 [-1.53,-1.52]) whereas wavelet scale 8 to scale 12 (temporal scales from 1 min to 14.9 min, with corresponding frequencies spanning from 1.12×10^{-3} Hz to 1.67×10^{-2} Hz) are fitted by a power law spectrum with a lower exponent -1.25[-1.42,-1.09] with uncertainties that exclude the IK value of $\alpha = -3/2$. This is again illustrated by extending the fitted line for scale 8 to scale 12 (temporal scales from 1 min to 14.9 min, with corresponding frequencies spanning from 1.12×10^{-3} Hz to 1.67×10^{-2} Hz). In this case, the '$1/f$' range is clearly identified at lower frequencies and is distinct from the lower frequency part of the IR. For comparison, we have taken the same spectra plotted in Figs. 3 and 4, and instead fitted a single power law to the range between wavelet scales R and P with temporal scales from 0.9 sec (1.11 Hz) to 30.0 min (5.56×10^{-4} Hz) and from 1.8 sec (0.56 Hz) to 14.9 min (1.12×10^{-3} Hz), respectively. This is shown in Figs. 5 and 6 respectively. The resultant exponents have an uncertainty that is reasonable (about 4%) but is larger than that obtained by fitting two spectral ranges (for the high-frequency ranges of Figs. 3 and 4, about 1%). Thus whilst we do not suggest these results provide an unambiguous discrimination between a single and dual scaling IR, it motivates the question of how often, and under what conditions, dual scaling may occur and be detected in the IR.

3.2. Spectral exponents survey

Both the range of scaling and the scaling exponent (Chen et al. 2020; Alberti et al. 2020) of the IR are known to evolve with distance from the Sun. To examine how the IR evolves with distance from the Sun and with plasma β in more detail, we have performed a scan of the first four PSP orbits and we list in Fig. 10 results for all intervals that satisfy our criteria for homoge-

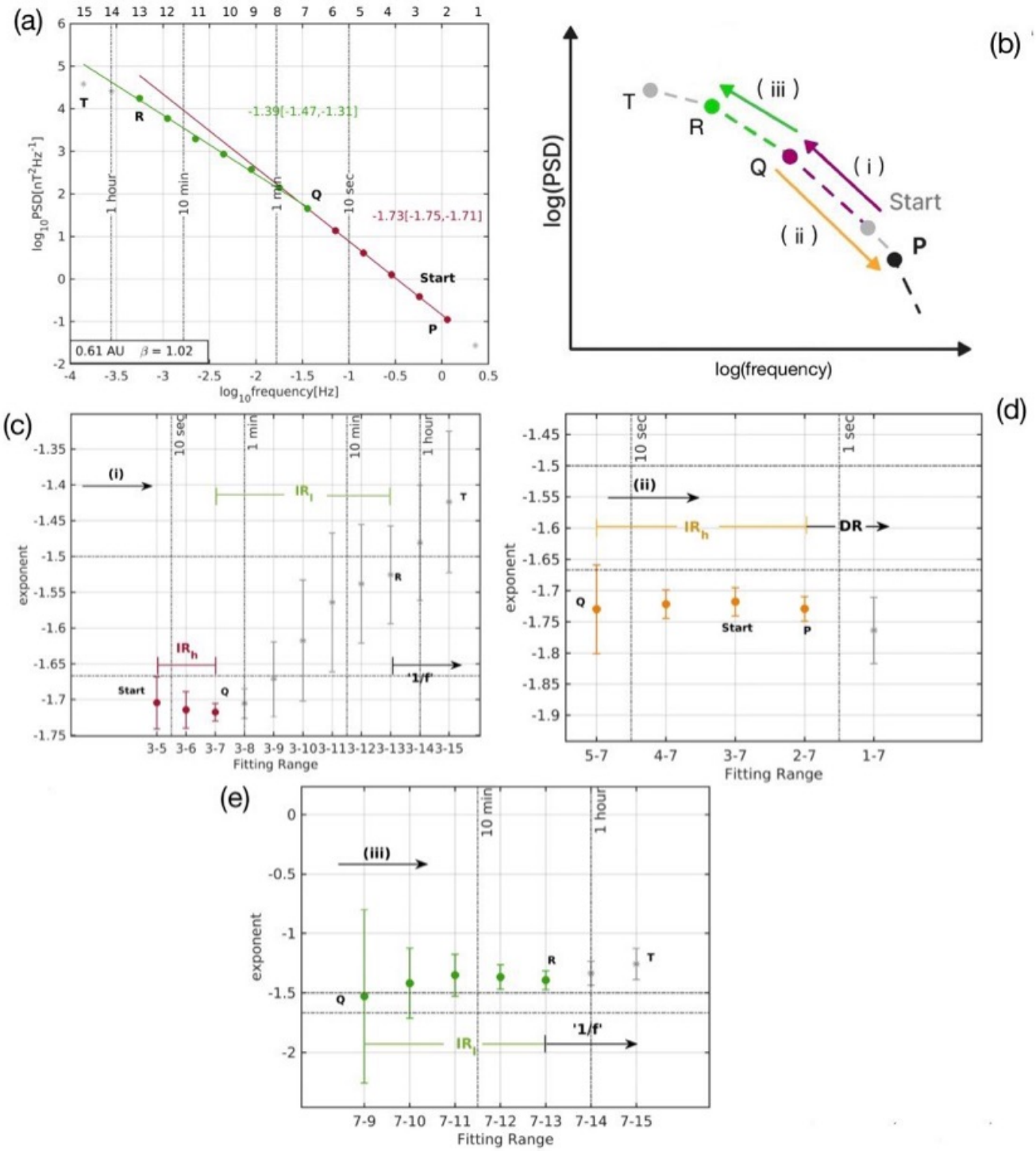

Fig. 3: Example of a type III spectrum which shows two ranges of scaling within the IR: close to Kolmogorov scaling at higher frequencies (red circles in top panel – light asterisks lie outside this range) and a shallower range (at lower frequencies (green circles in panel (**a**)). The interval is for PSP/FIELDS measurements of the full trace of power spectral tensor, taken over a 5-hour interval at 0.61 AU with local plasma $\beta = 1.02$. (**a**): Log-log plot of power spectral density versus frequency, the plotted points result from Haar wavelet analysis of the dataset. (**b**): Procedural diagram for the three plots below, used to identify the breakpoints between the three scaling ranges, together with their best-fit gradients. The first (counting from the right) red circle is labelled P. Breakpoints at the seventh point labelled Q (between gradients -1.73 and -1.39) and the at thirteenth point labelled R (between IR gradient -1.39 and '$1/f$'; the latter terminates at the fifteenth point, labelled T) are identified from the CI of the exponent using the method of Sec.2.2, that are displayed in the three plots below. (**c**): The minimum error is located at the seventh point, labelled Q, for pathway (i) extending from point 3 upwards (dark red). The continuation of pathway (i) beyond point 7 suggests a second breakpoint at point 13 where the CI suddenly increases. (**d**): Pathway (ii) descending from point 7 (yellow) has the minimum error when it encompasses points down to the second. (**e**): CI for pathway (iii), in green, confirms the breakpoint at point 13, labelled R.

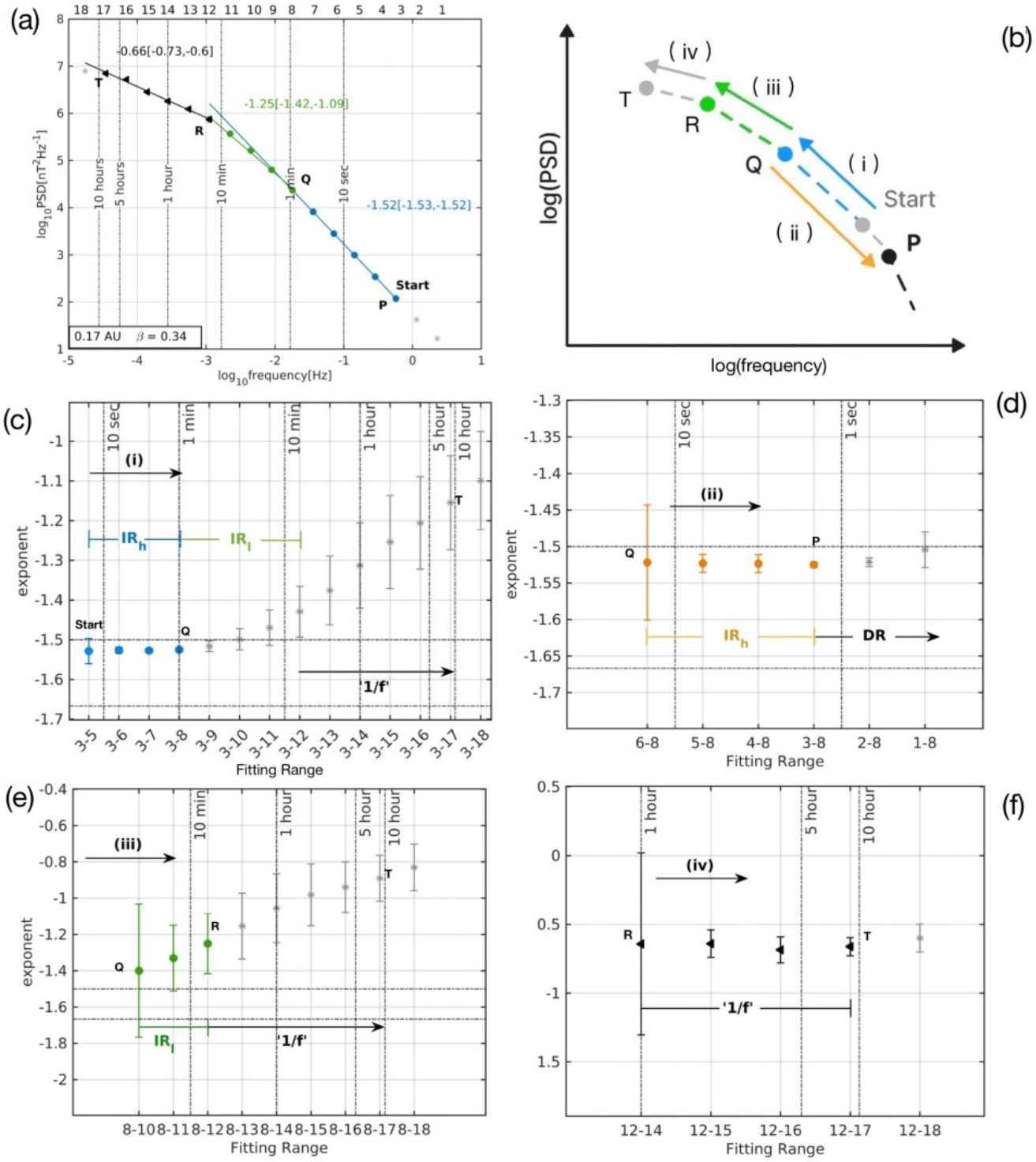

Fig. 4: Example of a type I spectrum which shows two ranges of scaling within the IR with an exponent close to IK at higher frequencies (blue circles in top panel) and a shallower range at lower frequencies (green circles in panel (**a**)). There is a transition '$1/f$' scaling at the lowest frequencies (black triangles in panel (**a**)). Interval is for PSP/FIELDS measurements of the full trace of power spectral tensor, taken over a 48-hour interval at 0.17 AU with local plasma $\beta = 0.34$. (**a**): Log-log plot of power spectral density versus frequency, the plotted points result from Haar wavelet analysis of the dataset. (**b**): Procedural diagram for the four plots, used to identify the breakpoints between three scaling ranges and their best-fit gradients. The first (counting from the right) blue circle is labelled P. Breakpoints at the eighth point labelled Q (between gradients -1.52 and -1.25) and the twelfth point labelled R (between IR gradient -1.25 and '$1/f$'; the latter terminates at the seventeenth point, labelled T) are identified from the CI of the exponent using the method of Sec.2.2, that are displayed the four plots below. (**c**): The minimum error is located at the eighth point, labelled Q, for pathway (i) extending from point 3 upwards (blue). The continuation of pathway (i) beyond point 8 suggests a second breakpoint at point 12 where the CI suddenly increases. (**d**): Pathway (ii) descending from point 8 (yellow) has minimum error when it encompasses points down to the third. (**e**): CI for pathway (iii), in green, confirms the breakpoint at point 12, labelled R. (**f**): CI for pathway (iv) shows that the '$1/f$' range continues to the seventeenth point, labelled T.

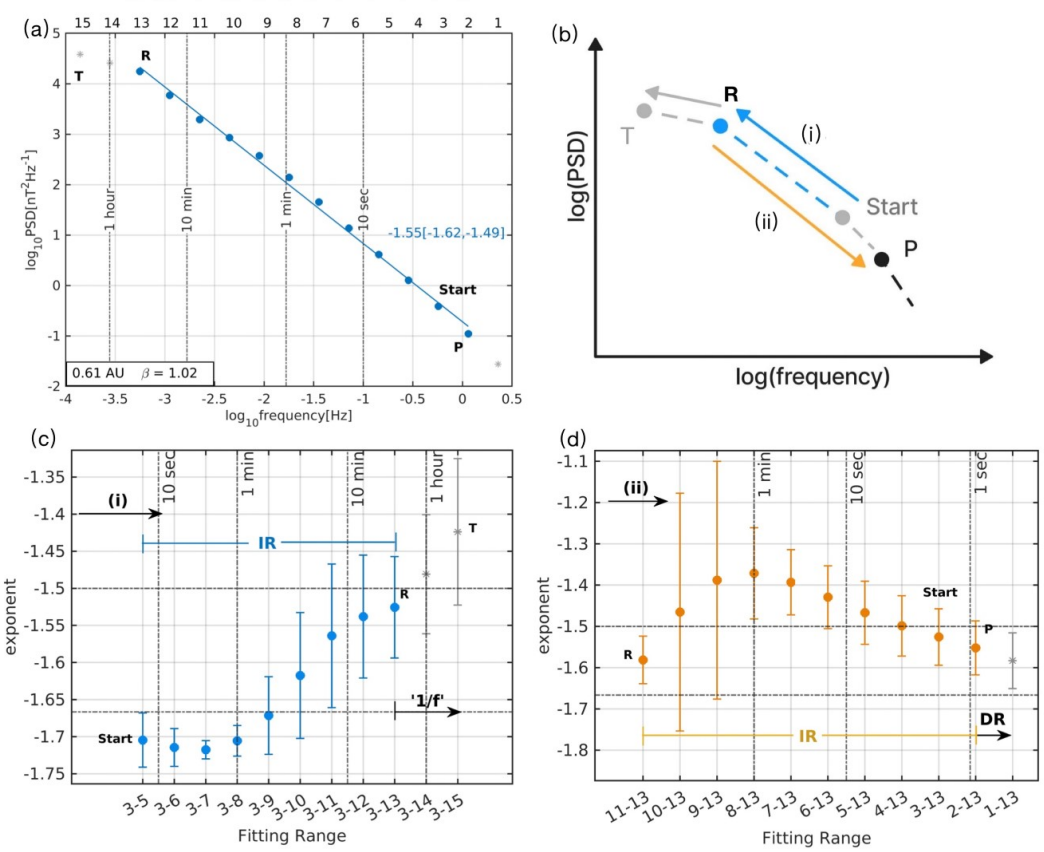

Fig. 5: Fit of a single gradient to the full IR of the data in Fig. 3. This fitting approach hides the well-defined breakpoint Q identified within the IR in Fig. 3, while still resulting in IK scaling within an acceptable margin of error (shown in blue). The wavelet points in the IR are denoted by blue circles. (**a**): Log-log plot of power spectral density versus frequency, the plotted points result from Haar wavelet analysis of the dataset. (**b**): Procedural diagram for the two plots below, used to identify the breakpoints between the three scaling ranges, together with their best-fit gradients. The first (counting from the right) blue circle is labelled P. Breakpoints at the thirteenth point labelled R (between IR gradient -1.55 and '$1/f$'; the latter terminates at the fifteenth point, labelled T) are identified from the CI of the exponent using the method of Sec.2.2, that are displayed in the two plots below. (**c**): Spectral exponent and its CI, on the blue pathway labelled (i) beginning at "Start" and ending at R in the procedural diagram above. (**d**): Pathway (ii) descending from point 13 (yellow) has the minimum error when it encompasses points down to the second.

neous turbulence, and have a clearly identified cross-over to a kinetic range and a '$1/f$' range of scaling. The ranges of values of plasma β and distance from the Sun are plotted in Fig. 7.

A significant proportion of these intervals are found to have a breakpoint within the IR, and in these cases, the temporal scales of the dual scaling ranges found by the above procedure are listed. In all these cases we quantify the percentage uncertainty on the power law scaling exponents and, in the cases where our procedure finds a dual-range IR, we obtain the exponents and uncertainties both for a single range of scaling IR (a single power law) and a dual-range IR (two power laws). Looking across these, it can be seen that in some cases, the single power-law fit, and dual power-law fit, give comparable uncertainties. In other cases, however, the dual-power law fit gives lower uncertainty in the high-frequency scaling range.

Figs. 8 and 9 plot how the IR power law range scaling exponents are ordered by distance from the Sun and plasma β. The upper and middle panels of Figs. 8 and 9 plot the obtained spectral exponents with 95% confidence intervals as a function of distance from the Sun, the middle panels present a zoom-in of the upper panels. In those cases where a fully resolved '$1/f$' range is found, its exponent is plotted in the upper panel (green symbols). The '$1/f$' range scaling exponent shows significant variation between intervals, however, it is distinct from that found for the IR. These intervals where a distinct '$1/f$' range is clearly resolved are at locations spanning 0.17 AU to 0.70 AU, however, these all correspond to local plasma β values $\leq$ 2.5. Intervals, where an unbroken IR range of scaling with a single exponent is determined by the above procedure, are indicated with red symbols on the figures. The scaling exponents found for these cases are closer to IK scaling for distances $\leq$ 0.5 AU, but are closer to Kolmogorov scaling beyond 0.6 AU. Single unbroken IR scaling with exponents spanning Kolmogorov and IK values are found at all plasma β. In cases where the exponent is closer to Kolmogorov, the ideal $\alpha = -5/3$ value often lies well outside the uncertainties. These intervals that show a single unbroken IR of scaling are thus consistent with previous studies. DFT spectra identified a drift towards approximately Kolmogorov scaling with increasing distance from the Sun beyond 1 AU (Roberts 2010), and specifically with PSP, a drift from approximately Kolmogorov scaling at around 1 AU, to approximately IK scaling closer to the Sun (Chen et al. 2020). However, these previous studies identify a gradual change, whereas here, we see a transition between Kolmogorov and IK at a distance between 0.5 AU

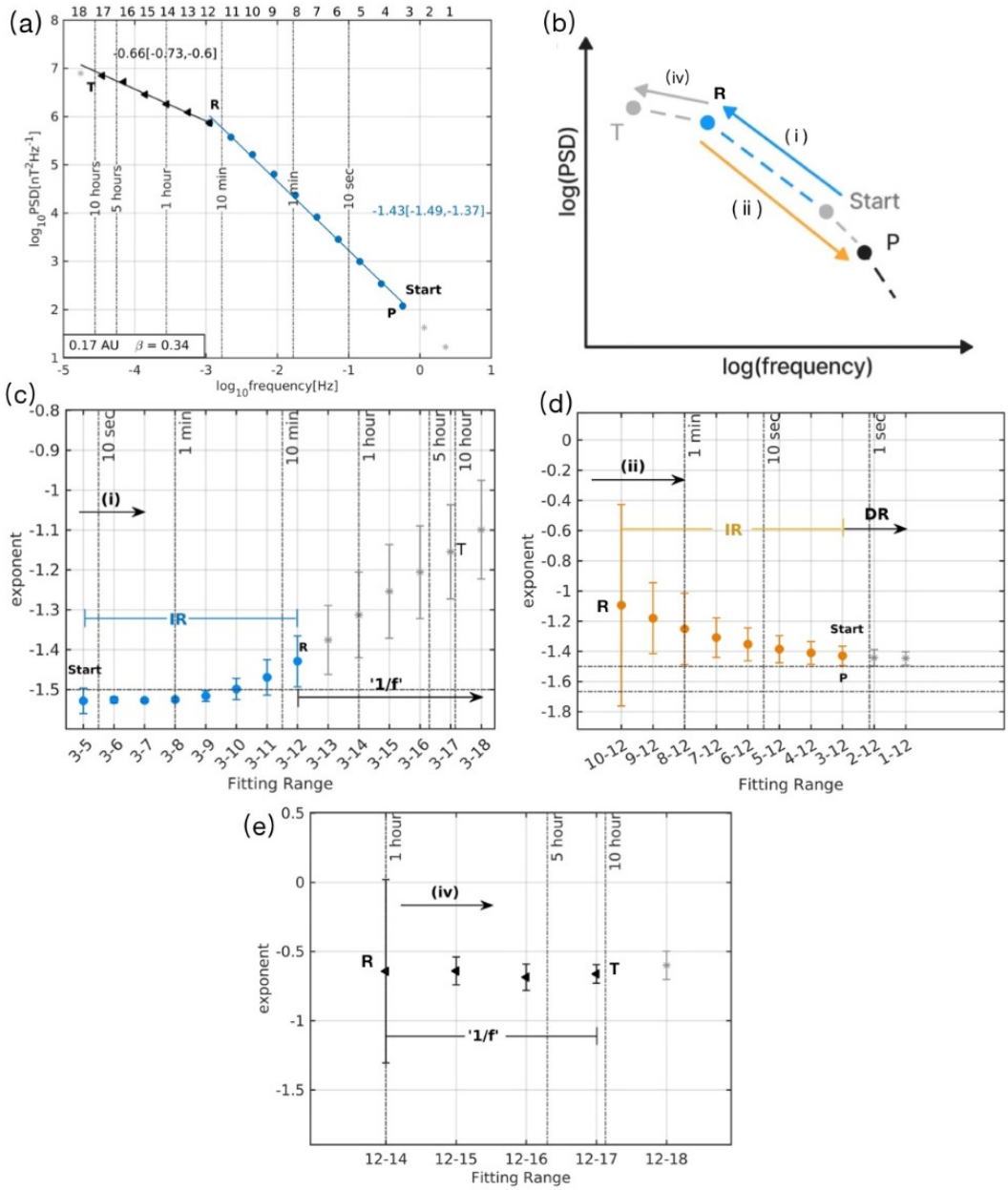

Fig. 6: Fit of a single gradient to the full IR of the data in Fig. 4, counterpart to Fig. 5 and 3. This fitting approach hides the well-defined breakpoint Q identified within the IR in Fig. 4, while still resulting in IK scaling within an acceptable margin of error (shown in blue). The wavelet points in the IR are denoted by blue circles, while black triangles represent those in the '1/f' range.

and 0.6 AU. These intervals sample a broad range of plasma β as shown in Fig. 9. The lower panels of Figs. 8 and 9 show the transitions to the '$1/f$' and dissipation ranges. The above methodology for detecting breakpoints identifies the first wavelet scale outside of the IR, so that the frequency of the transition to '$1/f$', and dissipation range, are respectively upper and lower bounds in frequency (the '$1/f$' can be at a lower frequency, the DR at a higher frequency). Irrespective of position and local beta, the high-frequency DR is close to 1 Hz, and the low-frequency '$1/f$' transition point corresponds to the period of a few minutes to an hour. Intervals, where our procedure identifies two distinct scaling ranges within the IR, are found at a range of distances from the Sun, but all occur for plasma $\beta \lesssim 1$. In contrast, single unbroken IR scaling is found at $\beta > 0.5$ (see Fig. 9).

The lower panels of Figs. 8 and 9 show where the breakpoint within the IR occurs in frequency, relative to the cross-over to the '$1/f$' and dissipation ranges. Importantly, these breakpoints within the IR are found with periods in the range of approximately 30 seconds to a few minutes, they are well separated in frequency and wavelet scale from the termination of the IR at the transitions to '$1/f$' and DR. In most of these cases we have identified a clear termination of IR scaling and transition to '$1/f$' regions of the spectrum, and in some cases, a clear power law '$1/f$' range. There are several possibilities for interpreting these IR spectra: (i) as two power law ranges with different exponents,

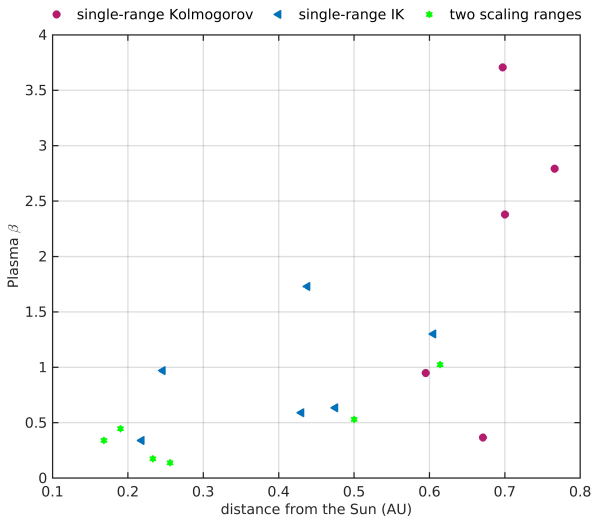

Fig. 7: Distribution of individual cases, categorized into three distinct types: single-range Kolmogorov (red circles); single-range IK (blue triangles); two-scaling range (green hexagrams). The x-axis denotes the distance from the Sun, while the y-axis represents the local plasma β value.

(ii) as a single power law range and (iii) as a monotonic deviation from the power law, as in the case of generalized similarity (Frisch 1995) which has been found in solar wind turbulence at the early stages of its evolution (Chapman & Nicol 2009). Interpretation (iii) may explain some of our results as in Fig. 8 we see that dual ranges of scaling within the IR are found within 0.3 AU, consistent with a less well-developed turbulent cascade. Interpretations (i) and (ii) for some intervals give essentially the same uncertainties so that 'Occam's razor' favours interpretation (ii), namely a single power law IR. However as detailed in Fig. 10, there are several cases where fitting two power law ranges significantly reduces the uncertainty in the exponent at higher frequencies, motivating further study. We emphasise the need for comparison, supported by uncertainty estimates, between the two distinct hypotheses of a single IR, and two IR ranges of scaling. Previous results, for example that of (Telloni 2022) have identified candidate dual-scaling IR spectra, however, this example was estimated by DFT and did not include uncertainty estimates on the spectral exponents.

In Figures 8 and 9, distinct scaling behavior was observed, leading to the classification of the results into four types. Type I spectra were found within a radial distance of 0.3 AU from the Sun. These spectra exhibited two distinct scaling ranges. The inner range, characterized by high frequencies, displayed scaling exponents consistent with the inertial range IK theory within the associated uncertainties. On the other hand, the outer range, representing lower frequencies, showed shallower scaling exponents ranging from -1.37 to -1.23. Type II spectra occurred between 0.4 and 0.5 AU. They displayed scaling exponents closer to, yet steeper than, the expected IK value of $\alpha = -3/2$. However, these exponents did not align precisely with the IK value within the estimated uncertainties. At two specific distances, namely 0.26 AU and 0.61 AU, Type III spectra were observed. They exhibited two distinct scaling ranges. The inner range, corresponding to higher frequencies, displayed an exponent of approximately -1.4. The low-frequency range, however, showed scaling behavior close to the Kolmogorov theory $\alpha = -5/3$. Notably, these spectra were found at the transitions between Type I and Type II, as well as between Type II and Type IV spectra. Beyond 0.5 AU from the Sun, Type IV spectra were observed. They displayed scaling exponents were close to, but mostly steeper than, the Kolmogorov prediction. The study also determined a lower bound on the frequency of the transition to the dissipation range, which was found to be approximately 1 Hz. Importantly, this lower bound remained unaffected by plasma β or the distance from the Sun. Furthermore, an upper bound on the frequency of the transition to the '$1/f$' range was established for all intervals considered in this study. Regarding the relationship between spectra types and plasma β, a tendency was observed for Type I spectra to be associated with $\beta < 1$. Conversely, Type IV spectra were observed across all values of β. However, it is worth noting that none of the intervals within 0.4 AU included high β values.

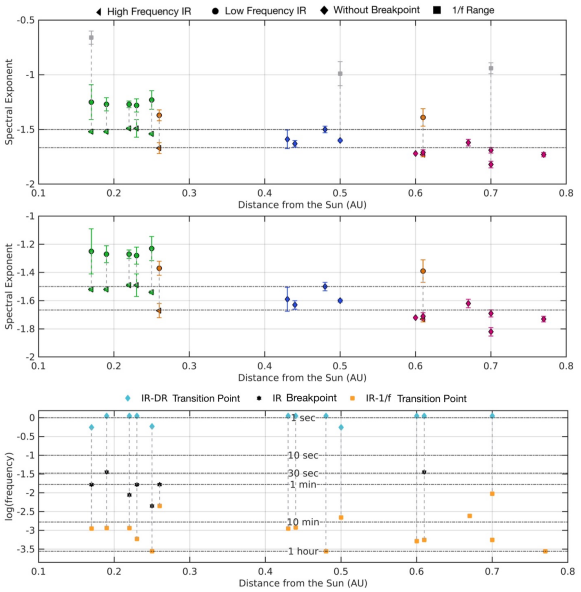

Fig. 8: Dependence on distance from the Sun of the fitted spectral exponents, and of the frequencies at which spectral breakpoints are found, for the trace of the power spectral tensor datasets of Figs. 1 to 4 and Fig. 10. Upper panel. Fitted spectral exponents plotted versus distance from the Sun, spanning 0.15 AU to 0.8 AU, for sub-ranges of the wavelet-derived spectrum which we have identified as: '$1/f$' (grey squares); type I spectra (green); type II spectra (blue); type III spectra (orange); type IV spectra (dark red); single IR (diamonds); IR containing a breakpoint, with exponents for the upper (triangles) and lower (circles) frequency ranges displayed separately. The horizontal dot-dash lines mark the IK(upper) and Kolmogorov (lower) values. Middle panel. Same as the top panel, but with '$1/f$' exponents excluded and covering a narrower range of exponent values between -1 and -2. Lower panel. Frequency limits of the IR identified as breakpoints to '$1/f$' scaling (yellow squares) and to the ion dissipation range (blue diamonds), together with frequency location of the breakpoint within the IR (black hexagrams) if found. Horizontal dot-dash lines indicate frequencies that correspond to oscillation periods between one second and one hour.

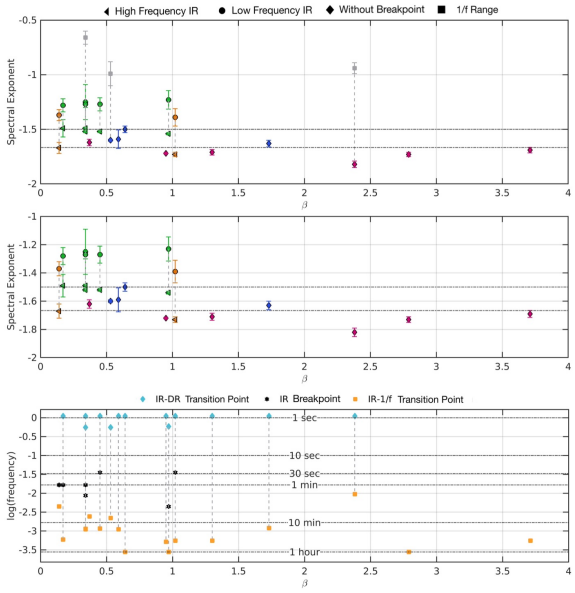

Fig. 9: Counterpart plots for Fig. 8, ordered with respect to the value of local plasma β instead of distance from the Sun.

4. Conclusions

Whilst it is well established that there is an inertial range (IR) of magnetohydrodynamic(MHD) turbulence in the solar wind, there has been considerable discussion of the value of the exponent of the observed power law power spectral density which varies with distance from the Sun (Chen et al. 2020; Roberts 2010). The value of the exponent is a key prediction of turbulence theories (Kraichnan 1965; Iroshnikov 1964; Kolmogorov 1941) as it is not universal (Chapman & Hnat 2007).

We have applied a systematic method to quantify the spectral breaks and scaling exponents from extended intervals of turbulence observed by PSP at different distances from the Sun and over a range of plasma β. Wavelets provide a natural tool for estimating the exponents of power law spectra as they provide a linear sampling of the log-frequency domain. We used UDWT Haar wavelet estimates of the power spectral density for multiple, long-duration intervals of uniform solar wind turbulence, sampled by PSP/FIELDS, selected to exclude coherent structures such as pressure pulses and current sheets, in which the primary proton population velocity varies by less than 20% of its mean value. Intervals are only included in the study where there is a clear identification of the approximately '$1/f$' range at low frequencies, an MHD IR of turbulence and a kinetic range, below the ion gyrofrequency.

We can characterize the spectra into four categories as follows:

1. Type I: Within 0.3 AU from the sun, the IR exhibits two distinct ranges of scaling. The inner, high frequency range has an exponent consistent with IK within uncertainties. The outer, low frequency range is shallower, with exponents in the range from -1.37 to -1.23.
2. Type II: Between 0.3 and 0.5 AU, the IR exponents are closer to, but steeper than, IK and do not coincide with the value $\alpha = -3/2$ within uncertainties.
3. Type III: At 0.26 AU and at 0.61 AU the IR has two distinct ranges of scaling. The inner, high frequency range has an exponent $\sim$ -1.4 and the low frequency range has an exponent close to Kolmogorov. These spectra are found at the transitions between Type I and Type II, and Type II and Type IV spectra.
4. Type IV: At distances beyond 0.5 AU from the Sun, the exponents are close to, but mostly steeper than, Kolmogorov: uncertainties inherent in the observed exponents exclude the value $\alpha = -5/3$.
5. We determine a lower bound on the frequency of the transition to the dissipation range at $\sim$ 1 Hz which is not sensitive to plasma β or distance from the Sun.
6. We determine an upper bound on the frequency of the transition to the '$1/f$' range in all intervals considered for this study.
7. There is a tendency for type I spectra to be found at $\beta < 1$ and for type IV spectra to be found at all β, however none of our intervals include high β within 0.4 AU.

Since the PSD-estimated scaling exponents are a central prediction of turbulence theories, these results provide new insights into the evolution of turbulence in the solar wind. We obtained estimates of the scaling exponents and scale breaks of the power spectra of MHD turbulence at sufficient precision to discriminate between Kolmogorov and IK turbulence, both within each spectrum and across multiple samples. Whilst we confirm the previously identified evolution from Kolmogorov-like scaling to IK-like scaling with decreasing distance from the Sun, the Kolmogorov-like values, which we find almost exclusively beyond 0.5 AU, are not in fact consistent with a $\alpha \approx -5/3$ spectral exponent within the fit uncertainties. Thus whilst the average over many spectral estimates at larger distances from the sun may approach an exponent of $\alpha \approx -5/3$, as found previously (Chen et al. 2020) the individual spectral exponents are not consistent with this value of the exponent. This is distinct from the behaviour within 0.5 AU where the exponents of each individual spectrum coincide with $\alpha = -3/2$ IK scaling, rather than in an average sense.

This discrepancy may arise due to the choice of magnetic field fluctuation coordinate system, and due to the anisotropic nature of these fluctuations, which we do not addressed here. Coordinate systems that align with a globally averaged background field (Matthaeus et al. 2012; Horbury et al. 2012; TenBarge et al. 2012, Zhao et al. 2022) or with a local scale by scale field that Kiyani et al. (2013) and Horbury et al. (2008) have both been proposed, as has binning the fluctuations with reference to the local field direction (Osman et al. 2014). Establishing whether working in these coordinate systems can systematically resolve the above discrepancy in how well Kolmogorov and IK scaling exponents will be the topic of future work. It raises the question, to what precision do we expect the observed power law exponents to agree with theoretical predictions in order to confirm a given turbulence phenomenology?

A transition between Kolmogorov and IK scaling within MHD IR scales at approximately 0.5 AU may be a distinct phenomenology of the solar wind at this heliospheric distance. There is some evidence that the effects of coronal events such as CMEs or coronal hole jets may be incorporated into turbulent solar wind at scales larger than 0.3 AU (Owens et al. 2017; Horbury et al. 2018). Alternatively, it may reflect, for example, the changes of the inbalance in IK turbulence (Galtier et al. 2001) or a varying level of the dynamic alignment between the magnetic field and the velocity fluctuations (Meyrand et al. 2016) at these scales.

We have found examples where the IR is well described by two power law sub-ranges with different scaling exponents. These breakpoints within the IR are found with periods in the range 30 seconds to 10 minutes. The breakpoints within the IR are well separated in frequency and wavelet scale from the termination of the IR at the transitions to '$1/f$' range and DR. Interpretations of these IR spectra include: two power law ranges with different exponents; a single power law range mostly with increased uncertainty particularly at higher frequencies; a monotonic deviation from power law. The suggestion of a two-power-law IR is currently tentative, and additional research is needed to clarify or resolve this matter. Specificially, the selection of an appropriate magnetic coordinate system requires further investigation. Nevertheless, these results motivate further study and emphasise the need for precise estimation of the power law exponents and their uncertainties as central to connecting these observations with theoretical predictions. A coexistence of IK and Kolmogorov turbulence within scales we traditionally refer to as MHD IR, is of importance in models of solar wind heating, see for example (Chandran et al. 2011).

Acknowledgements. We acknowledge the NASA Parker Solar Probe Mission, and the FIELDS team led by S. D. Bale, and the SWEAP team led by R. Kasper for use of data. The FIELDS experiment on the Parker Solar Probe spacecraft was designed and developed under NASA contract NNN06AA01C. SCC and BH acknowledge AFOSR grant FA8655-22-1-7056 and STFC grant ST/T000252/1. SCC acknowledges support from ISSI via the J. Geiss fellowship

References

Alberti, T., Laurenza, M., Consolini, G. et al. 2020, ApJ. 902, 84, https://dx.doi.org/10.3847/1538-4357/abb3d2
Bale, S., Goetz, K., Harvey, P. et al. 2016, Space Sci. Rev., 204, 49-82, https://doi.org/10.1007/s11214-016-0244-5
Barenblatt, G. 1996, Cambridge University Press
Bowen, T., Bale, S., Bonnell, J. et al. 2020, JGR Space Physics. 125, e2020JA027813, https://agupubs.onlinelibrary.wiley.com/doi/abs/10.1029/2020JA027813
Bruno, R. & Carbone, V. 2013, Living Rev. Sol. Phys., 2, https://doi.org/10.12942/lrsp-2013-2
Bruno, R., V. Carbone, L. Primavera et al. 2004, Ann. Geophys., vol. 22, no. 10, pp. 3751-3769. Copernicus GmbH, 2004.
Buckingham, E., 1914, Phys. Rev., 4, 345-376, https://link.aps.org/doi/10.1103/PhysRev.4.345
Chandran, B.D., Dennis, T.J., Quataert, E. et al. 2011, ApJ, 743(2), p.197.
Chapman. S, Nicol. R, 2009, Phys. Rev. Lett., 103, 241101, DOI: 10.1103/PhysRevLett.103.241101
Chapman, S. & Hnat, B. 2007, Geophys. Res. Lett., 34, https://agupubs.onlinelibrary.wiley.com/doi/abs/10.1029/2007GL030518
Chapman, S., Hnat, B., Rowlands et al. 2005, NPG, 12, 767-774, https://npg.copernicus.org/articles/12/767/2005/
Chen, C. H. K., L. Leung, S. Boldyrev et al. 2014, Geophys. Res. Lett., 41, 8081–8088, doi:10.1002/2014GL062009.
Chen, C.H.K. 2016, JPP, 82(6).
Chen, C., Bale, S., Bonnell, J. et al. 2020, ApJS, 246, 53, https://dx.doi.org/10.3847/1538-4365/ab60a3
Chen, C. H., Leung, L., Boldyrev, S et al. 2014, Geophys. Res. Lett., 41, 22, 8081–8088. https://doi.org/10.1002/2014GL062009
Davis, N., Chandran, B., Bowen, T. et al. 2023, ApJ, 950, 154, https://doi.org/10.48550/arXiv.2303.01663
Feynman, J. & Ruzmaikin, A., 1994, J. Geophys. Res. Space Phys., 99, A9, pp.17645-17651.
Fox, N., Velli, M., Bale, S. et al. 2016, SSR, 204, 7-48
Frisch, U. 1995, Astrophysical Letters And Communications.
Galtier, S., Nazarenko, S.V., Newell, A.C. et al. 2001, ApJ, 564, 1, p.L49
Gogoberidze, G. & Voitenko, Y.M. 2016, ApSS, 361, 11, pp.1-6
Goldreich, P. & Sridhar, S. 1995, ApJ, 438, pp. 763
Hnat, B., Chapman, S., Gogoberidze, G. et al. 2011, Phys. Rev. E., 84, 065401, https://link.aps.org/doi/10.1103/PhysRevE.84.065401
Horbury, T.S. & Balogh, A., 1997, NPG, 4(3), pp.185-199.
Horbury, T., Forman, M. & Oughton, S. 2008, Phys. Rev. Lett, 101, e175005
Horbury, T.S., Wicks, R.T. & Chen, C.H.K., 2012, Space Sci Rev, 172, pp.325-342.
Horbury, T.S., Matteini, L. & Stansby, D. 2018, MNRAS, 478, 2, pp.1980-1986.
Iroshnikov, P. 1964, Sov. Astron., 7 pp. 566
Kasper, J., Abiad, R., Austin, G. et al. 2016, Space Sci Rev, 204, 131-186, https://doi.org/10.1007/s11214-015-0206-3
Kiyani K.H., Osman K.T., Chapman S. 2015, Phil.Trans.R.Soc., A373: 20140155, http://dx.doi.org/10.1098/rsta.2014.0155
Kiyani, K., Chapman, S., Sahraoui, F. et al. 2013, ApJ, 763, 10, https://dx.doi.org/10.1088/0004-637X/763/1/10
Kolmogorov, A. 1941, Akademiia Nauk SSSR Doklady, 30 pp. 301-305
Kraichnan, R. 1965, Phys. Fluids, 8, 1385-1387
Longair, M. 2003, Cambridge University Press
Matthaeus, W.H., Breech, B., Dmitruk, P. et al. 2007, ApJ, 657, 2, p.L121.
Matthaeus, W.H., Servidio, S., Dmitruk, P. et al. 2012, ApJ, 750, 2, p.103.
Meyrand, R., Galtier, S. & Kiyani, K.H., 2016, PRL, 116, 10, p.105002.
Nicol R.M., Chapman S. C. Dendy R.O. 2009, ApJ, 703, 2138,(2009).
Osman, K., Kiyani, K., Chapman, S. et al. 2014, ApJL, 783, L27, https://dx.doi.org/10.1088/2041-8205/783/2/L27
Owens, M.J., Lockwood, M. Barnard, L.A., 2017, Sci. Rep., 7, 1, pp.1-6.
Parashar, T. & Matthaeus, W. 2022, Rev. Mod. Plasma Phys. 6, 41, https://doi.org/10.1007/s41614-022-00097-x
Politano, H., & Pouquet, A. 1995, Phys. Rev. E, 52, 1, p.636.
Roberts A. 2010, JGR https://doi.org/10.1029/2009JA015120
Salem, C., Mangeney, A., Bale, S.D. et al. 2009, ApJ, 702(1), p.537.
Sioulas, N., Huang, Z., Shi, C. et al. 2023, ApJL, 943, L8, https://dx.doi.org/10.3847/2041-8213/acaeff
Sorriso-Valvo, L., Marino, R., Lijoi, L. et al. 2015, ApJ, 807(1), p.86.
Telloni, D. 2022, Front. Astron. Space Sci., 9, https://doi.org/10.3389/fspas.2022.917393
TenBarge JM, Podesta JJ, Klein KG, Howes GG. 2012, ApJ,.753, 107. (doi:10.1088/0004-637X/753/2/107)
Tu, C. & Marsch, E. 1995, SSR, 73, 1-210, https://doi.org/10.1007/BF00748891
Verma, M. 1999, Phys. Plasmas, 6, 1455-1460
Verscharen, D., Klein, K. 2019, Living Rev. Sol. Phys., 16, 5 , https://doi.org/10.1007/s41116-019-0021-0
Wang, X., Chapman, S., Dendy, R. et al. 2022, 48th EPS Conference on Plasma Physics, https://indico.fusenet.eu/event/28/contributions/359/
Welch, P. D. 1967, IEEE trans. audio electroacoust., AU-15, 2: 70–73, doi:10.1109/TAU.1967.1161901
Wicks, R., Horbury, T., Chen, C. & Schekochihin, A. 2010, MNRAS, 407, L31-L35, https://doi.org/10.1111/j.1745-3933.2010.00898.x
Wicks, R., Forman, M., Horbury, T. & Oughton, S. 2012, ApJ, 746, 103, https://dx.doi.org/10.1088/0004-637X/746/1/103
Zhao, L., Zank, G., Adhikari, L. & Nakanotani, M. 2022, ApJL, 924, L5, https://dx.doi.org/10.3847/2041-8213/ac4415
Zhou, Y., Matthaeus, W. & Dmitruk, P. 2004, Rev. Mod. Phys., 76, 1015-1035 , https://link.aps.org/doi/10.1103/RevModPhys.76.1015

	a [b c]	$\frac{\lvert b-a\rvert}{a}\%$	$\frac{\lvert c-a\rvert}{a}\%$	IR Scale	β	d (AU)	Type
IR	–1.43[-1.49,-1.37]	-4.2	-4.2	1.8s-14.9min			
IR_h	-1.52[-1.53,-1.52]	-0.66	0	1.8s-1min	0.34	0.17	I
IR_l	-1.25[-1.42,-1.09]	-13.6	-12.8	1min-14.9min			
IR	-1.41[-1.46,-1.36]	-3.55	-3.55	0.9s-14.3min			
IR_h	-1.52[-1.53.-1.51]	-0.66	-0.66	0.9s-28s	0.45	0.19	I
IR_l	-1.27[-1.33,-1.21]	-4.72	-4.72	28s-14.3min			
IR	-1.43[-1.47,-1.4]	-2.8	-2.1	0.9s-14.5min			
IR_h	-1.49[-1.5,-1.47]	-0.67	-1.34	0.9s-1.9min	0.34	0.22	I
IR_l	-1.27[-1.3,-1.24]	-2.36	-2.36	1.9min-14.5min			
IR	-1.4[-1.45,-1.35]	-3.57	-3.57	0.9s-27.9min			
IR_h	-1.49[-1.57,-1.44]	-3.97	-3.31	0.9s-1min	0.17	0.23	I
IR_l	-1.28[-1.33,-1.22]	-3.91	-4.69	1min-27.9min			
IR	-1.45[-1.5,-1.4]	-3.45	-3.45	1.7s-60min			
IR_h	-1.54[-1.55,-1.53]	-0.65	-0.65	1.7s-3.7min	0.97	0.25	I
IR_l	-1.23[-1.32,-1.15]	-7.32	-6.5	3.7min-60min			
IR	-1.62[-1.67,-1.57]	-3.09	-3.09	0.4s-3.7min			
IR_h	-1.67[-1.72,-1.63]	-2.99	-2.4	0.4s-1min	0.14	0.26	III
IR_l	-1.37[-1.42,-1.32]	-3.65	-3.65	1min-3.7min			
IR	-1.59[-1.67,-1.5]	-5.03	-5.66	0.9s-14.9min	0.59	0.43	II
IR	-1.63[-1.66,-1.6]	-1.84	-1.84	0.9s-13.9min	1.73	0.44	II
IR	-1.5[-1.53,-1.47]	-2	-2	0.9s-60min	0.64	0.48	II
IR	-1.6[-1.61,-1.58]	-0.62	-1.24	1.8s-7.5min	0.53	0.50	II
IR	-1.72[-1.72,-1.71]	0	-0.58	0.9s-32min	0.95	0.60	IV
IR	-1.55[-1.62,-1.49]	-4.52	-3.87	0.9s-30min			
IR_h	-1.73[-1.75,-1.71]	-1.16	-1.16	0.9s-28s	1.02	0.61	III
IR_l	-1.39[-1.47,-1.31]	-5.76	-5.76	28s-30min			
IR	-1.71[-1.73,-1.68]	-1.18	-1.76	0.4s-29.6min	1.30	0.61	IV
IR	-1.62[-1.64,-1.6]	-1.23	-1.23	0.4s-6.8min	0.37	0.67	IV
IR	-1.82[-1.85,-1.78]	-1.65	-1.65	0.9s-1.8min	2.38	0.70	IV
IR	-1.69[-1.71,-1.66]	-1.18	-1.78	0.4s-29.6min	3.71	0.70	IV
IR	-1.71[-1.73,-1.69]	-1.17	-1.17	0.4s-60min	2.79	0.77	IV

Fig. 10: Details of each event, listed in order of increasing distance from the Sun, with fitted gradients of the wavelet spectrum and 95% confidence intervals for three categories with their percentage differences. IR scale is shown with events separated by lines. Cases with two IR ranges also show their high- and low-frequency IRs (IR_h and IR_l) and corresponding local plasma β, distance from the Sun (d) and type. All figures are obtained for the trace of the power spectral tensor.